Supplementary Information

Flexible Metamaterials with Near-Infrared Chirality Fabricated by 1D Multi-pen Tip-based Lithography

Jeong-Sik Jo[a†,‡], Jihoon Cho[b,‡] , Chiwon Choi[a], Heeso Noh[b]*, and Jae-Won Jang[a,c,d]*

---

[a] Division of System Semiconductor, Dongguk University, Seoul, 04620, Republic of Korea. E-mail: jwjang@dgu.ac.kr

[b] Department of Nano and Electronic Physics, Kookmin University, Seoul, 02707, Republic of Korea. E-mail: heesonoh@kookmin.ac.kr

[c] Department of Physics, Dongguk University, Seoul, 04620, Republic of Korea.

[d] Institute for Next-Generation Semiconductor Technology (INGST), Dongguk University, Seoul, 04620, Republic of Korea.

†Present address: Advanced Bio and Healthcare Materials Research Division, Korea Institute of Materials Science (KIMS), Changwon, Gyeongnam, 51508, Republic of Korea

‡The authors contributed equally to this work.

I. Comparison of nanofabrication methods for metasurface/metamaterial fabrication

Table S1. Comparison of representative nanofabrication approaches (resolution, throughput, and relative complexity) relevant to metasurface/metamaterial pattern definition.

Technique	Typical lateral resolution	Patterning mode	Typical throughput	Vacuum	Mask	Relative complexity in infrastructure	Relevance to metasurfaces/ metamaterials
Electron-beam lithography (EBL) [1]	Sub-10 nm (state-of-the-art); ~10 nm commonly reported	Serial direct-write	Low	Yes	No (maskless)	High (vacuum e-optics; resist process; maintenance)	Gold standard for prototyping and master-mold fabrication; limited for large-area production
Nanoimprint lithography (NIL) [2,3]	Sub-10 nm; replication capability down to sub-3 nm reported	Parallel replication (step-and-repeat / wafer imprint)	High	No (typically)	Yes (master mold)	Medium–High (imprint tool and high-quality mold; overlay needs)	High-volume replication once mold exists; suited to large-area metasurfaces
Direct laser writing (DLW) / 2-photon polymerization (2PP) [4]	Down to ~100 nm commonly; sub-100 nm reported (optimized)	Serial voxel scanning (3D additive)	Low	No	No (maskless)	Medium–High (fs laser and precision optics; material constraints)	Excellent for true-3D prototyping/masters; throughput limits large-area periodic arrays
Multi-pen tip-based lithography (TBL) [5-7]	Sub-100 nm catalyst patterning under ambient conditions (typical)	Parallel direct-write using a multi-pen probe array	Medium; ~scales with number of pens (N)	No	No (maskless)	Low–Medium (ambient, vacuum-free; probe-array tool)	Parallel catalyst patterning for solution-based etching (e.g., MACE) and rapid iteration; compatible with release/transfer to flexible substrates

**Values indicate commonly reported capabilities and qualitative throughput trends; actual performance might depend on tool configuration, pattern density, and process conditions*

[1] W. F. van Dorp, B. van Someren, C. W. Hagen, P. Kruit and P. A. Crozier, *Nano Letters*, 2005, **5**, 1303-1307.

[2] D. K. Oh, T. Lee, B. Ko, T. Badloe, J. G. Ok, and J. Rho, *Front Optoelectron*, 2021, **14**, 229-251.

[3] S. V. Sreenivasan, *Microsystems & Nanoengineering*, 2017, **3**, 17075.

[4] Z. Faraji Rad, P. D. Prewett and G. J. Davies, *Microsystems & Nanoengineering*, 2021, **7**, 71.

[5] G. Liu, S. H. Petrosko, Z. Zheng, and C. A. Mirkin, *Chemical Reviews*, 2020, **120**, 6009-6047.

[6] J. Haaheim, R. Eby, M. Nelson, J. Fragala, B. Rosner, H. Zhang, and G. Athas, *Ultramicroscopy*, 2005, **103**, 117-132.

[7] This work

II. Detailed fabrication procedure for quasi-3D Si chiral structure encapsulated in PDMS

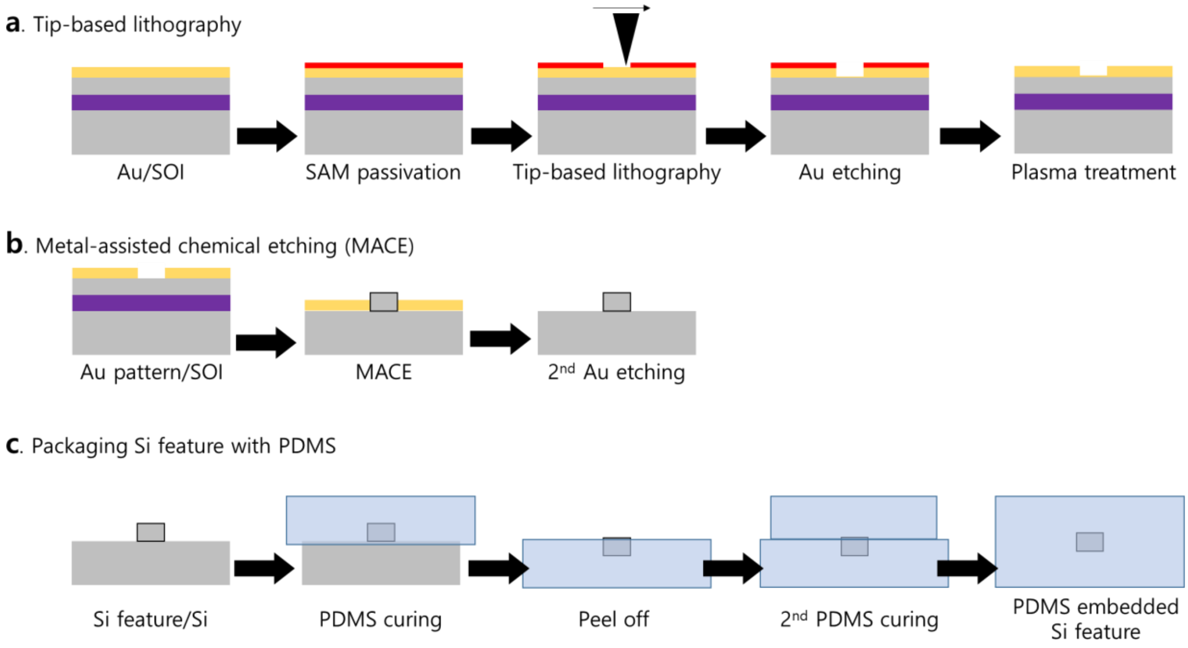

Figure S1. Schematic diagrams illustrating every step in the fabrication process of quasi-3D Si chiral structures encapsulated in PDMS.

III. Fabricated Si chiral structures and PDMS-assisted separation from the substrate

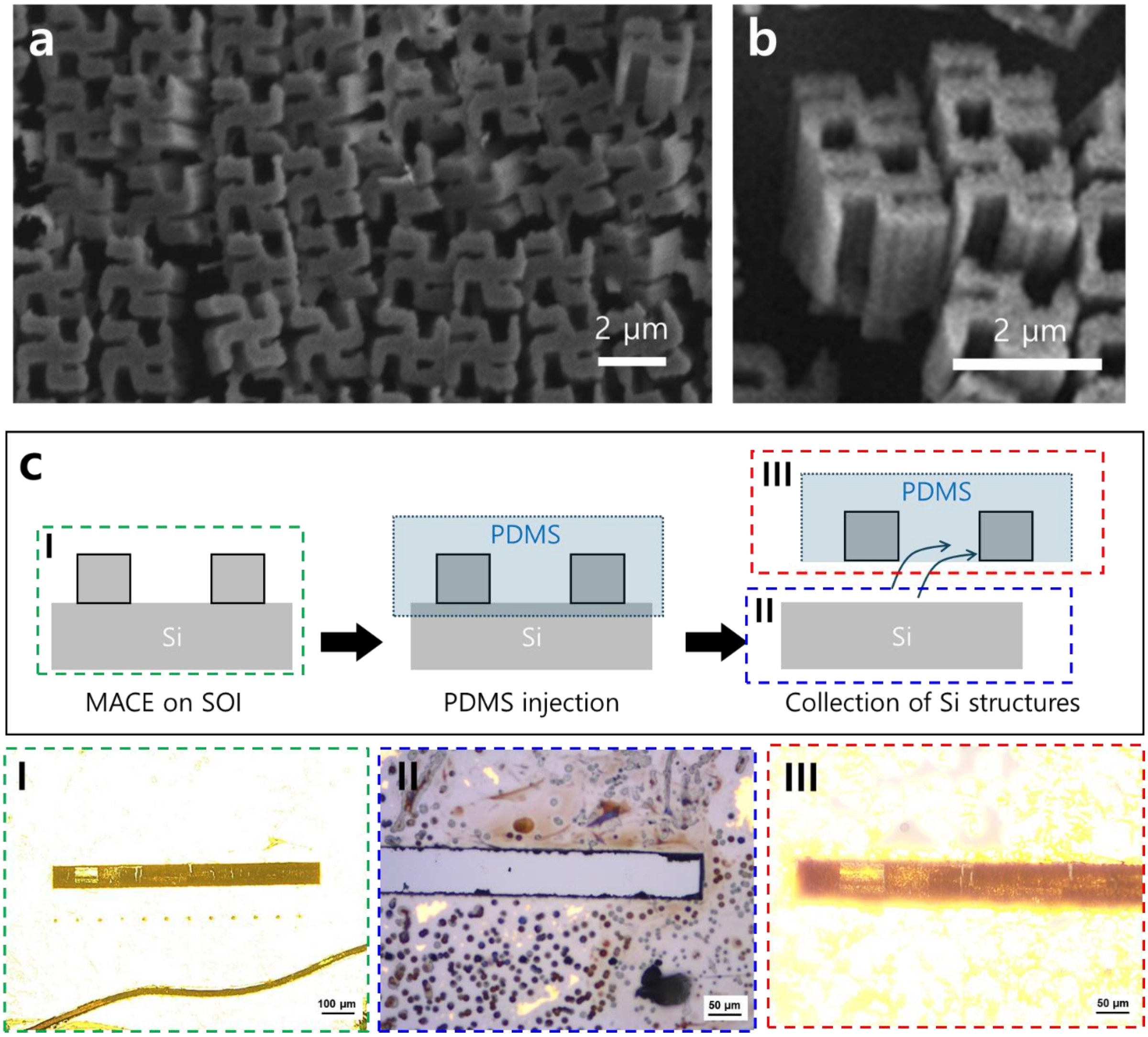

Figure S2. a-b) SEM images of Si chiral structures detached from the substrate following MACE on an SOI wafer. c) Schematic illustrating the separation of Si chiral structures from the substrate using PDMS. Steps I, II, and III are indicated in c.

IV. Designed pattern for counterclockwise-chiral fylfot

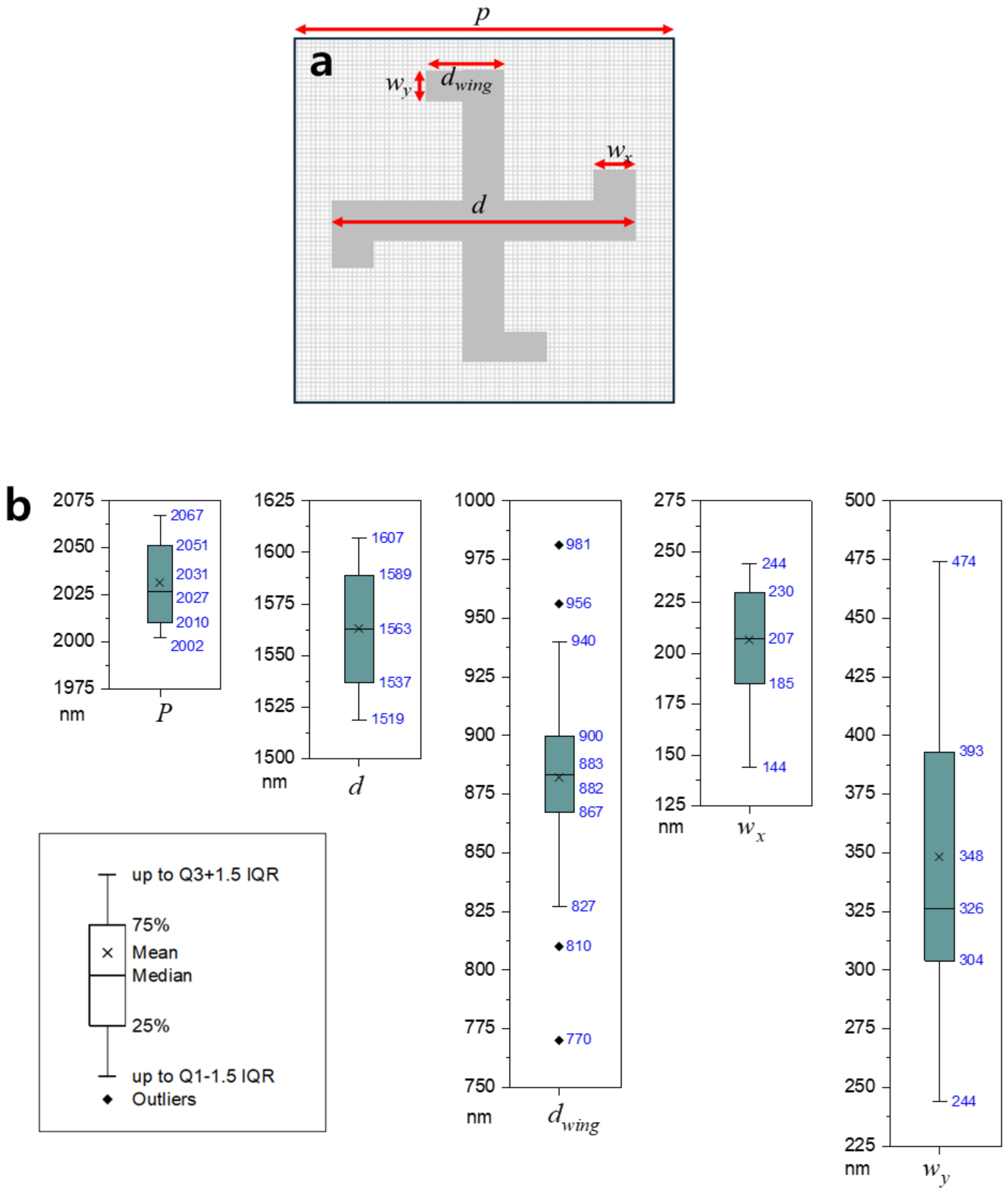

Figure S3. a) Designed a pattern for a counterclockwise-chiral fylfot. Critical design parameters are marked with symbols. d is the size of fylfot, p *is* the unit-cell size, d_{wing} is the length of the wing of fylfot, w_x and w_y are the widths of the perpendicularly and horizontally bended ends at the fylfot structures, respectively. b) Box chats for the designed parameters with experimentally observed dimensional variations in the fabricated Si fylfot structures. The data for the parameters are obtained from direct measurements of the SEM images.

V. AFM tip contamination after repeated dot-patterning

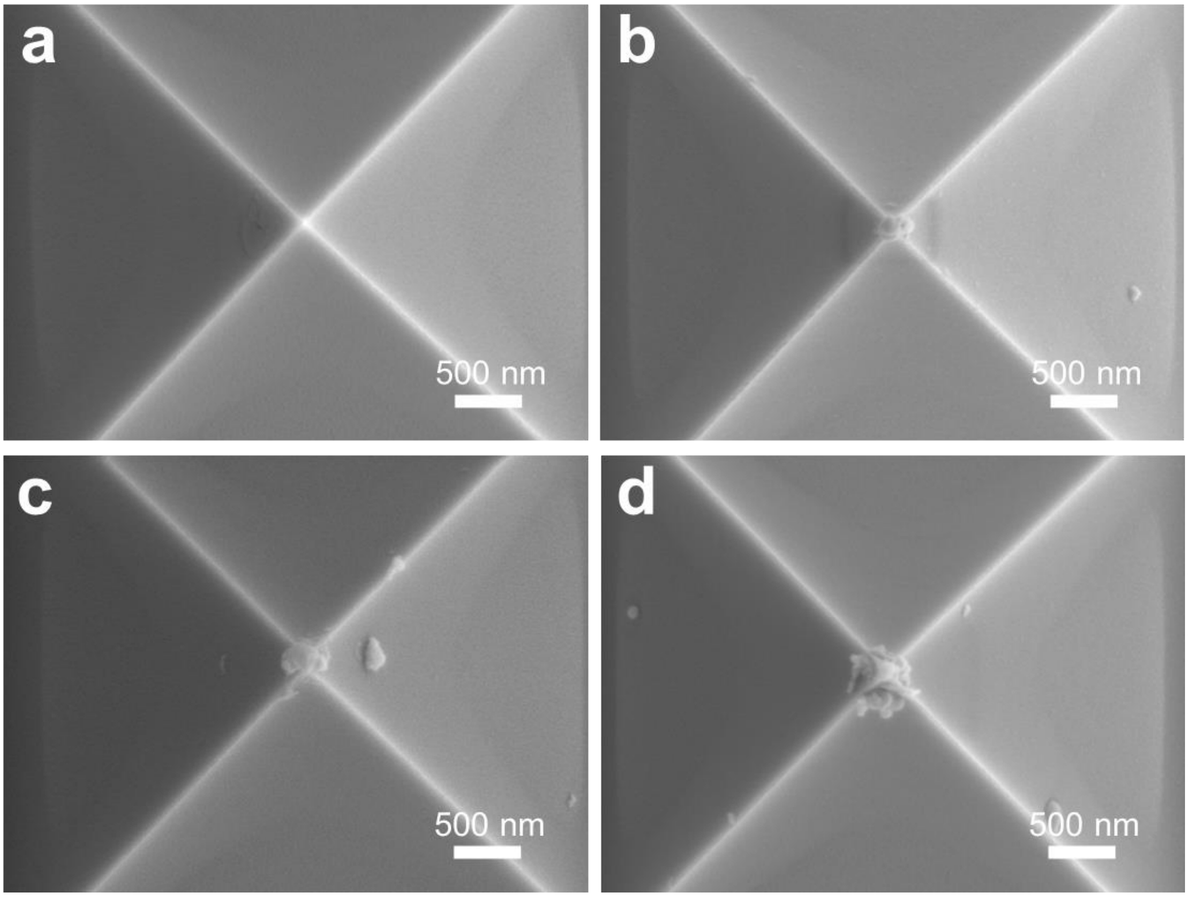

Figure S4. SEM images of the AFM tip apex after repeated dot-patterning: a) pristine tip before patterning; b) after 10,890 patterns; c) after 33,000 patterns; and d) after 66,000 patterns.

VI. Experimental spectra of the normalized intensity of LCP and RCP without bending of the sample

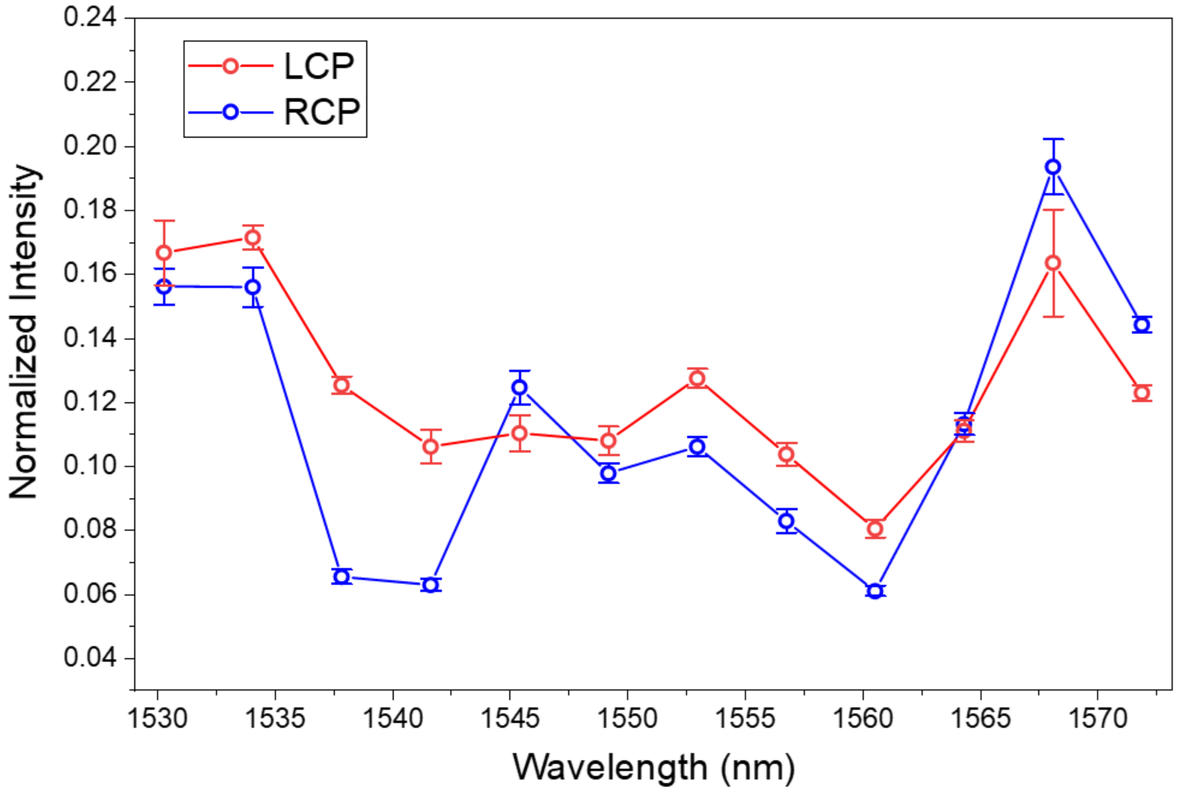

Figure S5. Normalized intensity of LCP (red circle) and RCP (blue circle) without bending of the sample.

VII. CD spectra dependent on in-plane anisotropy of the counterclockwise-chiral fylfot

An effective wavelength-scale thickness is important for exhibiting chiro-optical responses at normal incidence [Zhu et al., Light: Science & Applications 7 (2018) 17158]. Cavity-like standing-wave conditions in high-index dielectric platforms can drive out-of-plane displacement-current loops that generate effective in-plane magnetic moments, thereby enabling intrinsic chirality at normal incidence. Thus, the cavity-like performance of the quasi-3D Si fylfot structures would be anticipated due to the thickness of Si fylfot structures (> 1600 nm), the Si refractive index (n_{Si} = 3.48), and the wavelength in use (λ ~1550 nm). The corresponding effective wavelength of our samples should be about 445 nm (λ/n_{Si} = 1550 nm/3.48), which is short enough for the thickness of quasi-3D Si fylfot structures and in which the effective in-plane magnetic moments would be generated.

In addition, the in-plane anisotropy of the Si fylfot structure can contribute to the normal-incidence chiral response of the sample. To characterize it, CD spectra with different w_x/w_y ratios have been obtained (Figure S6). The w_x/w_y ratios are chosen based on experimentally observed dimensional variations in the fabricated Si fylfot structures (Figure S3). The CD spectra dramatically change as the w_x/w_y ratio varies. In detail, the CD spectrum of 0.8 (w_x/w_y ratio) represents the blue-shifted peak and the negative contrast compared to that of the sample without in-plane anisotropy (w_x/w_y ratio 1.0), which are also observed in the experimentally observed CD spectrum for the Si fylfot encapsulated in PDMS (Figure 3c). Considering the resemblance between the CD spectra obtained by the experiment and simulation, it is assumed that the in-plane anisotropy of the Si fylfot structure contributes to the chiral response of the sample. Therefore, it can be concluded that the effective wavelength-scale thickness and the in-plane anisotropy of the Si fylfot structure result in chiro-optical responses of the quasi-3D Si counterclockwise-chiral fylfot encapsulated in PDMS at normal incidence.

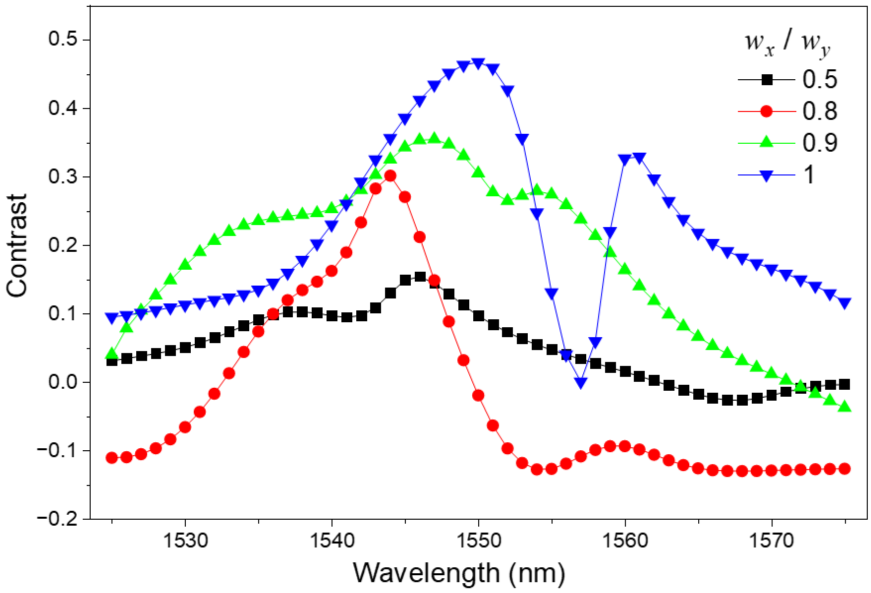

Figure S6. CD spectra for the quasi-3D Si counterclockwise-chiral fylfot encapsulated in PDMS, as the ratio (w_x/w_y) between the widths of the perpendicularly (w_x) and horizontally (w_y) bended ends at the fylfot structures changes in order of 0.5, 0.8, 0.9, and 1.0.

VIII. Optical accessories for bending of the flexible chiral metamaterials

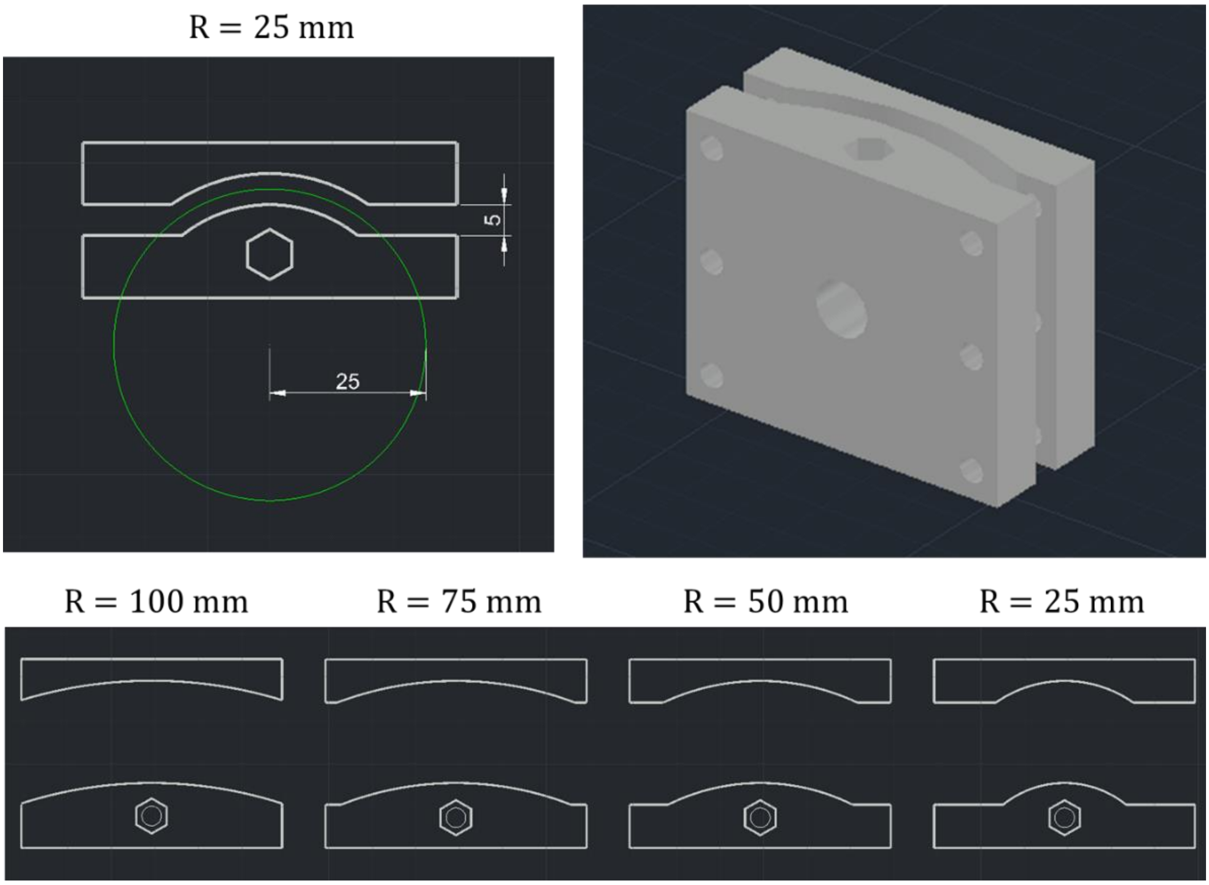

Figure S7. Schemes of optical accessories for bending flexible metamaterials

The accessories to control the degree of bending of the structure were made on a 3D printer (Sindoricoh, DP203, Korea). Figure S7 shows the schematic of the optical accessory (AutoCAD Academic license). To numerically represent the degree of bending, which is denoted by the angle of the arc ($\theta \propto 1/R$). Therefore, as the radius R of the circle increases, the angle of the arc decreases, and the degree of bending decreases. In total, four accessories are created with different R values, corresponding to $1/R$ = 0.04, 0.02, 0.013, and 0.01. Flat has $R = \infty$, so $1/R$ = 0.

IX. The detailed model and simulations for the bending measurement configurations

Even under the maximum bending condition (R = 25 mm), the illumination condition in our measurement can be regarded as effectively near-normal. Specifically, the maximum lateral length of the flexible patterned metamaterials is ~640 μm, and the maximum lateral length is perpendicular to the bending axis of the optical accessories for the bending of flexible metamaterials. Owing to the flexible patterned metamaterials being put in the middle of the bending platform, the normal incidence changes should be the maximum at the end of the patterned metamaterials (half of the maximum lateral length, ~320 μm = 0.32 mm). For the smallest radius of curvature used (R = 25 mm), the corresponding local surface tilt across the illuminated region is estimated as $\theta \approx s/R = 0.32\ \text{mm}/25\ \text{mm} \approx 0.0128\ \text{rad} \approx 0.73°$, as shown in Figure S8. Therefore, the incidence-angle deviation remains well below 1°, supporting the assumption of near-normal incidence for all bending measurement configurations.

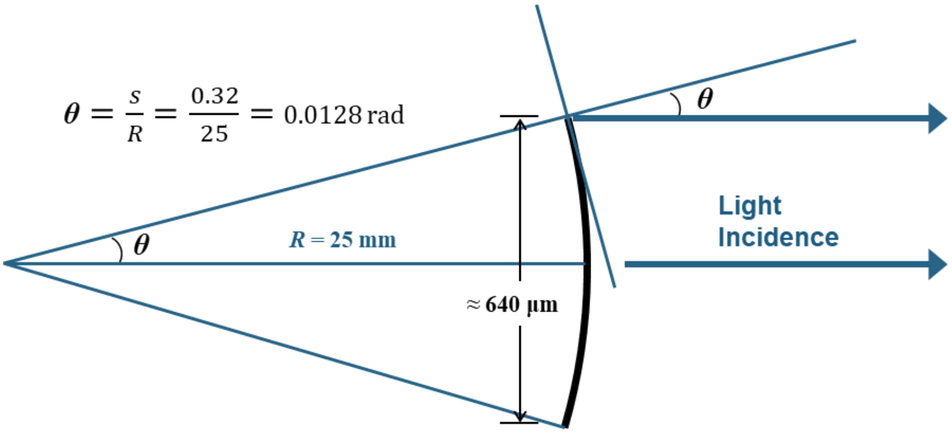

Figure S8. A scheme for the normal incidence changes in the flexible patterned metamaterials with the maximum lateral length of 640 μm, bending by the smallest radius of curvature (R = 25 mm).

In Figure S9, the incidence-angle- and wavelength-dependent CD spectra for the quasi-3D Si counterclockwise-chiral fylfot encapsulated in PDMS are shown as a 3D map and a graph, respectively. The contrast between the intensities of LCP and RCP, that is $(I_L - I_R) / (I_L + I_R)$, is obtained by simulation as the incidence angle (θ) changes from 0° to 1° with a step of 0.1°. The CD spectra do not change dramatically with a change in normal incidence. Therefore, the incident light is fixed at the normal direction, and only the periodicity in the direction of bending is considered as the parameter to characterize the bending effect of the chiral structures.

In addition, the effect of lowering the sample's refractive index on the CD spectrum is characterized. Figure S10 shows that the blue-shifted CD spectra for the quasi-3D Si counterclockwise-chiral fylfot encapsulated in PDMS (without bending), as the refractive index of silicone decreased from 3.478 to 3.373 in steps of 0.001. A 2 nm blue shift of the CD spectra is observed, corresponding to a 0.005 decrease in the refractive index of silicone.

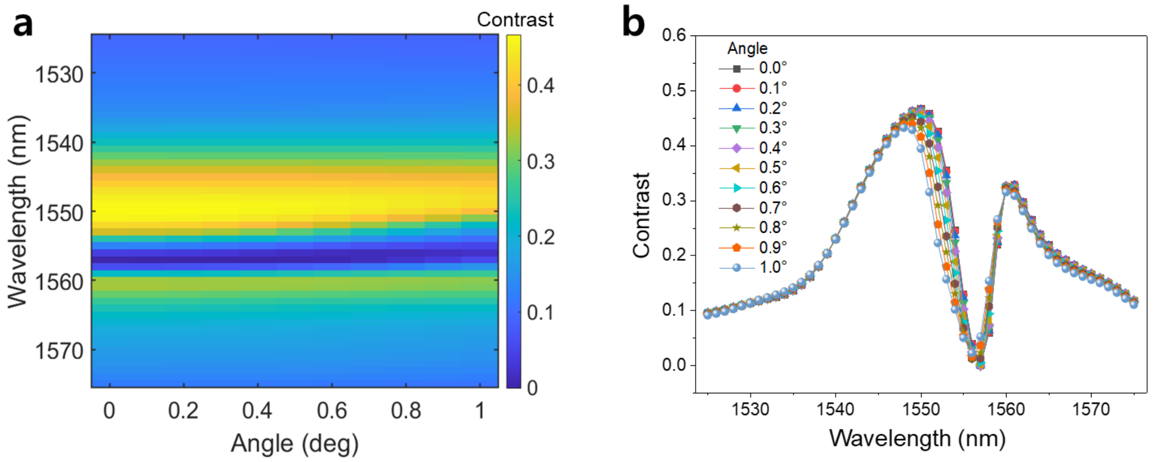

Figure S9. The simulated incidence angle- and wavelength-dependent CD (contrast) a) map and b) graph for the quasi-3D Si counterclockwise-chiral fylfot encapsulated in PDMS as the incidence angle changes from 0° to 1° with a step of 0.1°. The CD spectra change slightly; the peak near 1550 nm slightly decreases and blue-shifts as the incidence angle increases.

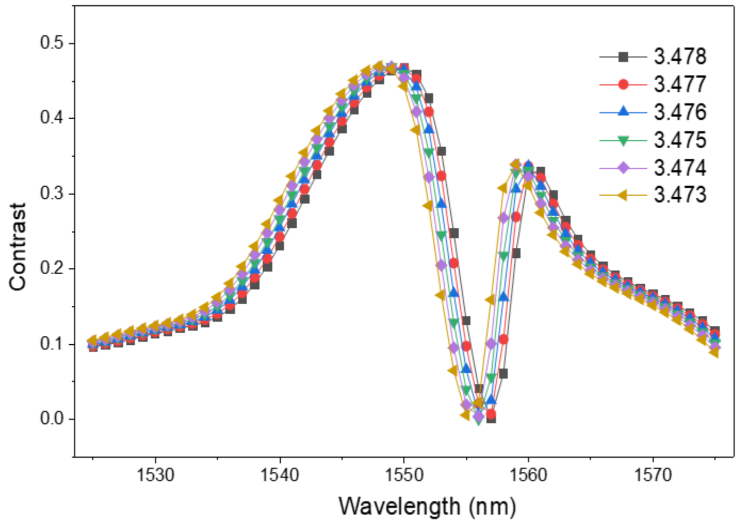

Figure S10. CD spectra for the quasi-3D Si counterclockwise-chiral fylfot encapsulated in PDMS as the refractive index of silicone decreased from 3.478 to 3.473 in steps of 0.001. The CD spectra show a blue shift as the refractive index of silicone decreases.

X. CD spectra of the flexible chiral metamaterials bent with a different radius of curvature (R = 100 mm)

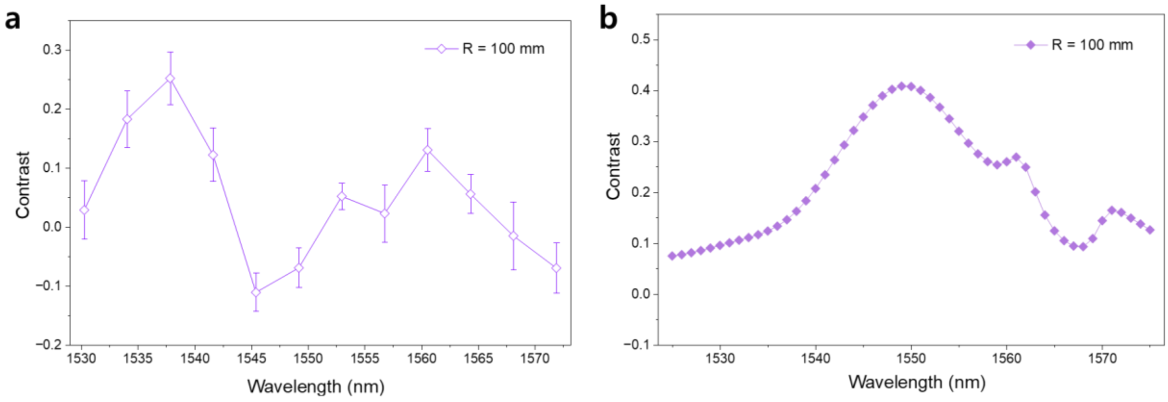

Figure S11. a) Experimental and d) simulated CD spectra for a fabricated metamaterial inserted into a bent optical accessory with R = 100 mm.